Radio-Frequency Ion Thrusters—Power Measurement and Power Distribution Modeling

Published in Journal of Propulsion and Power, DOI: 10.2514/1.B36868

C. Volkmar[a], C. Geile[b], and K. Hannemann[c]
Spacecraft Department, Institute of Aerodynamics and Flow Technology, German Aerospace Center, Bunsenstrasse 10, 37073 Goettingen, Germany

We present a methodology to measure the power delivered to sustain an inductive plasma discharge inside radio-frequency ion thrusters. This measurement is performed in real time near the coil within the resonant circuit using a patented low-noise radio-frequency voltage and current sensor system. With knowledge of the actual forwarded power, the efficiency of the generator under consideration, including the power feed cable, is assessed in real time. The variation of the power-to-thrust ratio can thus be understood more clearly since its value is given by physical changes of the plasma properties as well as the quality of the impedance bridge between the generator and plasma load. The latter can directly be determined by the proposed methodology, while the influence of the plasma parameters on the power-to-thrust ratio is obtained by means of a numerical model that is used in postprocessing to assess the power distribution within the thruster.

I. Introduction

Electric propulsion is now of substantial interest for modern space flight. The application spectrum of electric thrusters ranges from the station keeping and orbit raising of satellites to interplanetary space flight [1–3].With the appearance of all-electric communication satellites, the importance of electric propulsion has recently moved farther into the foreground, primarily due to its superior mass usage efficiency compared to chemical propulsion. Those satellite platforms also offer enough power on the spacecraft to release the full potential of electric propulsion in terms of propulsive force [4].

Electric propulsion assemblies are constituted by the thruster itself and several peripheral devices supplying it with propellant, power, and operational signaling. Those devices are often combined in dedicated power supply and control units PSCUs [5]. Performance optimization strategies are therefore ideally implemented at the assembly level, which gradually transforms the historically rather scientific view of those thrusters to a systems engineering view.

With this work, we want to introduce an approach that helps us to better understand the interaction of radio-frequency (RF) ion thrusters (RITs), electric thrusters of particular interest for this work, with their radio-frequency generators (RFGs). The RFG is a crucial part of the PSCU of a RIT assembly, but there is little information available, if any at all, that describes the impact the two systems have on each other. In our approach, we want to make it clear that the RFG has a significant influence on the overall power balance of a RIT assembly.

A. State of the Art

Radio-frequency generators used for RITs are typically composed of a half-bridge topology, which is operated in the near-resonant mode around $1-2\,\mathrm{MHz}$ [6]. The actual choice of operating frequency f is a function of the inductive discharge parameters and thus the dimensions of the coil and plasma chamber d. Roughly, an antiproportional correlation can be assumed; i.e., $f \propto 1/d$. The

[a] Electric propulsion test facility engineer, chris.volkmar@dlr.de
[b] Electric propulsion test facility technician, christopher.geile@dlr.de
[c] Head of Spacecraft Department, klaus.hannemann@dlr.de

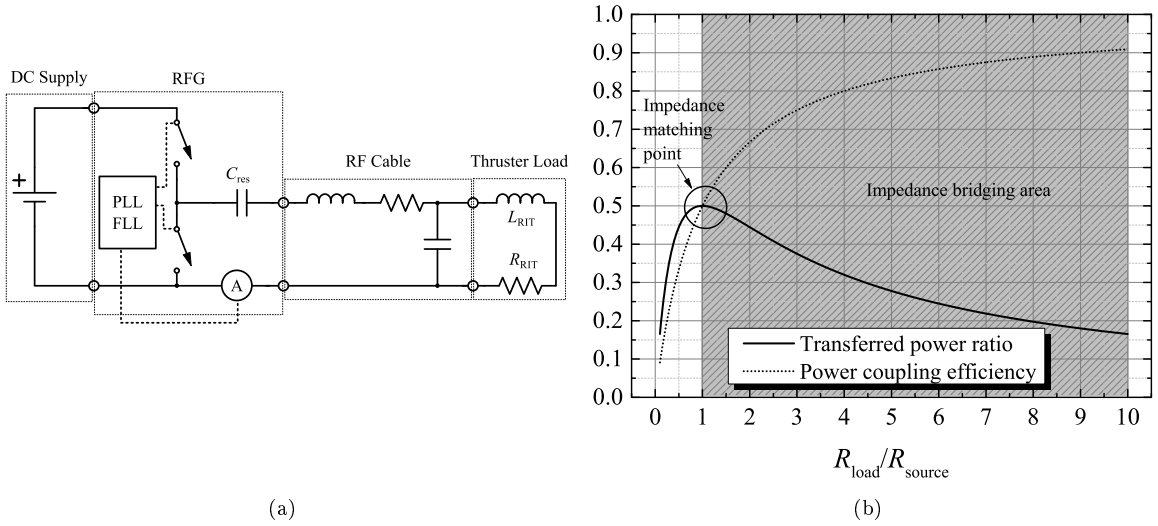

Fig. 1 a) Typical diagram of a RIT powered within a resonant circuit and b) comparison of purely ohmic matched and bridged impedances.

thruster itself is composed of the previously mentioned induction coil, which is typically wrapped around a cylindrical, trapezoidal, or hemispherical discharge chamber. Additionally, a set of either two or three extraction grids is attached to the discharge vessel and used for electrostatic ion extraction. More details on the design of a RIT can be found in [7,8].

A basic propulsive system assembly includes the thruster and the PSCU, which is subdivided into the RFG, a DC power supply for the RFG, a mass flow controller, and DC power supplies for positive high voltage (PHV) and negative high voltage (NHV) for the extraction grid system. The RFG is attached to the antenna coil surrounding the thruster using a coaxial or triaxial feeding cable. In this configuration, the thruster is driven within a resonant circuit consisting of the inductance of the thruster L_{RIT}, an equivalent ohmic resistance R_{RIT} that includes plasma, coil wire and eddy current losses, and a series capacitance C_{res} that is part of the output stage of the RFG. The control logic of the RFG is based on a phase-locked-loop/frequency-lockedloop scheme that tends to switch one of the transistors when the current measured in the return line is near zero, as depicted in Fig. 1a. This method is referred to as zero-current switching and is used to efficiently transfer power to a load if the source has small output resistance [9]. This methodology is known as impedance bridging and enables transfer efficiency greater 0.5; i.e., $\eta = P_{\mathrm{RF}}/P_{\mathrm{DC}} > 0.5$. In contrast to impedance matching, which is commonly used in 50 Ohm-RF systems with $\eta \approx 0.5$, it is possible to overcome severe power loss within the generator in the bridging mode [10]. Figure 1b shows the quantitative comparison of both operating regimes. The impedances will be exactly matched if $R_{\mathrm{source}} = R_{\mathrm{load}}$, given that both load and source impedances show only ohmic behavior. In the case of $R_{\mathrm{source}} < R_{\mathrm{load}}$, as indicated in the figure by the shaded area, the impedances are bridged. This implies that the transferred power is not at its maximum, which enables power transfer efficiency greater than 0.5. Impedance bridging is sometimes referred to as loading reduction [11].

B. Proposed Methodology

Since the load of the previously defined resonant circuit is defined by the plasma parameters it comprises a highly dynamic behavior if the thruster is driven in different operational modes, e.g., transition from low- to high-thrust mode. Depending on the relation R_{RIT}/R, with R denoting the output resistance of the generator including the RF cable, the efficiency of the power coupling will be affected, which ultimately leads to power loss in the generator/cable. Since most scientists and engineers only refer to the power drawn from the DC supply P_{DC}, it can be misleading when assessing performance data of the thrusters such as the power-to-thrust ratio (PTTR).

Here, we want to differentiate between the DC power and the actual RF power that is forwarded to the thruster to sustain the plasma discharge at given points of operation by means of phase-

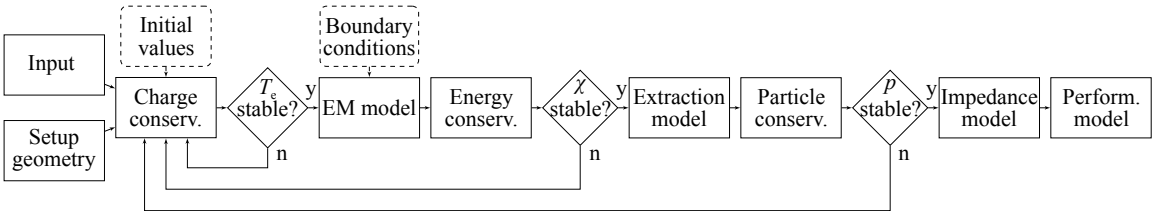

Fig. 2 Flow chart of the numerical model. It consists of three conservation equations (charge, energy, and mass conservation) that are iteratively brought to convergence.

resolved power measurement. The experimental setup and the methodology are described in Sec. III in more detail. The accurate power measurement was achieved by an Impedans Poly OctivVI sensor that is available commercially. This device has the advantage of low insertion loss and thus a minimal impact on the resonant circuit itself. Previous attempts, such as presented in [12], always suffered from unstable latency and phase shift between voltage and current sensors and hence exhibited large error bars if the experiments were not conducted in thermal equilibrium. It is evident that this is not always possible due to different processes such as mode transitions or even the diurnal thermal cycle.

With the experimentally measured RF power, a direct statement about coupling efficiency is possible with

$$\eta = \frac{P_{\mathrm{RF}}}{P_{\mathrm{DC}}}. \tag{1}$$

The remaining power $P_{\mathrm{DC}} - P_{\mathrm{RF}} = (1-\eta)\, P_{\mathrm{DC}}$ is lost within the generator and feeding cable and currently cannot be divided any further. However, since the semiconductor junction resistance is commonly known from data sheets, an approximate relation of the losses may be deduced from that. Here, however, we will instead focus on the power transferred to the thruster with the aid of numerical modeling. With this model, which is explained in more detail in Sec. II, we can furthermore divide P_{RF} into several channels of loss. Those are typically wire and eddy current loss, ionization and excitation loss, wall flux and sheath potential loss, and elastic, Coulomb, and stochastic collision losses.With this methodology, it is therefore possible to exactly reveal the power distribution of the complete assembly, which is considered very valuable for optimizing system performance and creating input parameters for thermal analyses that additionally aim to increase the system quality.

II. Model Overview

A flow chart of the model developed is shown in Fig. 2. In the following, the model is introduced, including a description of its working principle, basic assumptions used, and the most important features for the actual study. The input into the model is given by the working point parameters of the thruster; i.e., propellant mass flow $\dot{V}$ in standard cubic centimeters per minute (sccm), voltages for the screen grid V_{scr}, and acceleration grid V_{acc}, respectively, extracted ion beam current I_{b}, and neutral gas (and thruster housing) temperature T_{n}. All other important quantitites, such as coil current, applied frequency, and plasma parameters, are calculated within the model. The model's complete architecture and other detailed information can be found in [13,14].

The assumptions made within the proposed model correspond to those used within the vast majority of volume-averaged models [15–21] that mostly follow Lee and Lieberman's [22] approach, at least to a certain extent. Those assumptions are summarized as follows.

The cold gas approximation is used; i.e., neutrals and ions are assumed to be in thermal equilibrium with the wall temperature ($T_{\mathrm{n}} = T_{\mathrm{i}} = T_{\mathrm{w}}$). This is due to the typically low ionization fraction in inductively coupled discharges as well as the high elementary weight of the xenon ions, which are commonly used as propellant, that makes them practically invariant to the quickly oscillating electric field induced by the coil.

Electrons are assumed to have a Maxwellian distribution in phase space. Therefore, the electron temperature can be used to express the mean kinetic energy of the electrons. The plasma is assumed

to be quasi-neutral within the bulk region; i.e., $n_\mathrm{e} = n_\mathrm{i}$. This is, however, not true in the sheath area where $n_\mathrm{i} > n_\mathrm{e}$. The sheath area is not resolved in the electromagnetic part of this code.

Only singly charged xenon ions are assumed. Because of the low electron temperature (typically in the area of $2 - 5\,\mathrm{eV}$), the chance to have electrons reach the second ionization potential of xenon is very small. No secondary electron emission from the surfaces touching the plasma is assumed due to the low mean electron temperature.

The pre-sheath region is not included in the electromagnetic model. That region is necessary for pre-acceleration of ions toward the sheath in order to give them enough kinetic energy to reach the Bohm velocity at the sheath edge. Otherwise, they would not be able to surpass the potential barrier. In the code, ions at the sheath edge are assumed to have reached the Bohm velocity $u_\mathrm{B} = (kT_\mathrm{e}/m_\mathrm{i})^{1/2}$ instantaneously, with k denoting Boltzmann's constant and m_i denoting the ionic mass.

The following collisions are taken into account: elastic electron-neutral collisions, elastic electron-ion collisions, elastic ion-neutral collisions, inelastic electron-neutral collisions (excitation and ionization), and stochastic collisions as defined in [15].

Electron heating in the H mode only is assumed due to comparably high degrees of ionization [17]. Typically, an inductive discharge is sustained by both capacitive and inductive heating, going from the E mode to H mode with an increasing degree of ionization (which is caused by an increasing coil current). The degree of ionization is still low, typically in the order of $10^{-4} - 10^{-2}$, regardless of the actual heating mode of the discharge. Because of the assumption of explicit H mode heating, the electrical behavior of the plasma load is represented by an inductive-ohmic impedance.

All of these assumptions apply for the plasma model, which is regarded as the core of the self-consistent treatment. The self-consistent solution begins with the input of the axi-symmetric geometry of the thruster consisting of a discharge chamber, an extraction grid system, thruster housing, and other conducting parts within the assembly. In axi-symmetric systems, $\partial/\partial\phi = 0$ holds true, with ϕ denoting the azimuthal component.

A. Charge Conservation

First, a charge conservation equation that relates the volume ionization rate to the loss of charge to the walls is solved:

$$K_\mathrm{iz} n_\mathrm{n} = \frac{u_\mathrm{B}}{d_\mathrm{eff}} \tag{2}$$

In this equation, K_iz denotes the Maxwellian-averaged rate constant for ionization, and d_eff denotes the effective bulk plasma size that is iteratively calculated with an analytic expression for the plasma sheath thickness. After convergence, the mean Maxwellian electron temperature can be obtained analytically. The cross-sections for the collisions are taken from [23,24].

B. Energy Conservation

Energy conservation is achieved if the deposited electromagnetic power in the plasma, which is calculated by the electromagnetic model, equals the power lost to collisions:

$$\frac{1}{2} \iiint_V \left|\widetilde{\mathbf{E}}\right|^2 \mathrm{Re}\,\kappa_\mathrm{p}\,\mathrm{d}V = P_\mathrm{coll} \tag{3}$$

In this Eq. (3), $\widetilde{\mathbf{E}}$ denotes the induced electric field. The link between the plasma and electromagnetic model is given by the conductivity κ_p, which again is determined by the plasma parameters:

$$\kappa_\mathrm{p} \approx \frac{\epsilon_0 \omega_\mathrm{pe}^2}{\nu_\mathrm{en,eff}^2 + \omega_\mathrm{eff}^2} \left(\nu_\mathrm{en,eff} - \mathrm{i}\omega_\mathrm{eff}\right) \tag{4}$$

In this equation, ϵ_0 denotes the vacuum permittivity and ω_pe denotes the electron plasma frequency; i.e., the collective response of electrons to the excitation by electric fields. Furthermore, $\nu_\mathrm{en,eff}$ denotes the effective electron-neutral collision frequency, which is given by $\nu_\mathrm{en,eff} = \nu_\mathrm{en} + \nu_\mathrm{ei} + \nu_\mathrm{stoc}$, and ω_eff the electron effective RF oscillation frequency. This effective frequency slightly differs from

the applied RF due to electron kinetic processes. The effective frequency is calculated following an approach described in [25].

C. Electromagnetic Coupling

The governing equation within the electromagnetic model is the time-harmonic quasi-stationary diffusion equation [26]:

$$\nabla \times \left(\frac{1}{\mu} \nabla \times \widetilde{\mathbf{A}} \right) + \mathrm{i}\omega\kappa\widetilde{\mathbf{A}} + \widetilde{\mathbf{J}}_\mathrm{s} = \mathbf{0} \tag{5}$$

This is assumed valid for RITs because the wavelength of the applied current signal through the coil is typically orders of magnitude larger than the coil wire. Therefore, radiation will only play a minor role. In this equation, $\widetilde{\mathbf{A}}$ denotes the phasor of the vector potential field, $\widetilde{\mathbf{J}}_\mathrm{s}$ denotes the phasor of the source current density field, and $\mu = \mu_0\mu_\mathrm{r}$ denotes the permeability, with the vacuum permeability μ_0 and the relative permeability μ_r, of the media within the simulation domain. In the axisymmetric representation, only the azimuthal component of the vector potential field is of interest, leading to $\widetilde{\mathbf{A}} = \widetilde{A}_\phi \mathbf{u}_\phi$, with $\mathbf{u}_\phi$ denoting the unit vector in the azimuthal direction. The conductivity is defined per Eq. (4) in plasma regions. Conductivities of metallic structures are also implemented as a function of material and temperature, following the relation

$$\kappa\left(T\right) = \frac{1}{\rho_0 \left[1 + \alpha \left(T - T_0\right)\right]}, \tag{6}$$

with ρ_0 denoting the electrical resistivity at temperature T_0 and α denoting an empirical fit parameter. Information on both can be found for various metals in many databases, e.g., provided by the National Institute of Standards and Technology. For this study, the temperatures of the discharge vessel, the neutral gas, and all metallic structures except the induction coil are fixed at 100 °C or 120 °C, depending on the extracted beam current. There are four temperature sensors attached to significant structural points of the thruster that verify these values. The induction coil is actively water cooled at 10 °C. This is taken into account in the model. The conductivity is assumed to be isotropic; no magnetic confinement is modeled.

The solver for the vector potential is based on a finite-difference representation of Eq. (5), which is not further explained in this paper. Since the presheath region is not modeled, there is no scalar potential distribution, which in reality exists due to ambipolar diffusion, and the electric field can be calculated from

$$\widetilde{E}_\phi = -\mathrm{i}\omega\widetilde{A}_\phi. \tag{7}$$

The magnetic flux density field in axi-symmetric coordinates is given by:

$$\widetilde{\mathbf{B}} = \left(\frac{\widetilde{A}_\phi}{r} + \frac{\partial \widetilde{A}_\phi}{\partial r} \right) \mathbf{u}_z - \frac{\partial \widetilde{A}_\phi}{\partial z} \mathbf{u}_r \tag{8}$$

The induced eddy currents (in the plasma as well as in other conducting media) are furthermore obtained by Ampère's law:

$$\widetilde{J}_\mathrm{ind} = \frac{\partial \widetilde{H}_r}{\partial z} - \frac{\partial \widetilde{H}_z}{\partial r} \tag{9}$$

The displacement current term is neglected due to quasi-stationary time dependence of the fields.

With the axi-symmetric representation, high resolution in the $r-z$ plane is achievable. Features such as the impact of the skin and proximity effect in the coil wire can thus be taken into account, while the model can still be run on a standard desktop computer. The skin effect is caused by the current density in the conducting wire, which is induced in the direction opposite of the source current density. In contrast to that, the proximity effect is, in principle, the skin effect mutually caused in adjacent coil windings. It is almost impossible to find analytic solutions for the impact of the proximity effect if nonideal geometries are considered, as is the case here due to the thruster

housing and the plasma that both consist of conductive media that have to be taken into account. Therefore, it is regarded as beneficial that the diffusion equation intrinsically covers this effect by means of the lossy media term [26]. As a result of those two effects, the resistance of the coil wire will be affected by current displacement (skin effect) and crowding (proximity effect), which are both functions of the complex geometry and the applied RF. The resistance of the coil determines the coupling efficiency from coil to plasma and is thus a very important measure for the performance of a RIT.

To have the electromagnetic model calculate the correct deposited power density within the plasma, a realistic representation of the plasma density distribution, which ultimately determines the distribution of conductivity, is modeled using heuristic profiles introduced and verified in [27]. The distribution H follows a parabolic shape defined by

$$H = \sqrt{\left[1 - \left(\sqrt{1-h_r^2}\,\frac{r}{r_0}\right)^2\right]\left[1 - \left(\sqrt{1-h_z^2}\,\frac{z}{z_0}\right)^2\right]}, \tag{10}$$

with h_r and h_z denoting the density bulk-to-sheath-edge ratios [22]. Those ratios highly depend on the discharge parameters T_e and p and are therefore iteratively calculated as well.

With the deposited power, Eq. (3) can be solved for n_e until the convergence of the ionization fraction $\chi = n_\mathrm{e}/\left(n_\mathrm{e} + n_\mathrm{n}\right)$, which closes the second loop depicted in Fig. 2.

D. Particle Conservation

The next conservation equation to be solved is the particle balance that relates the amount of particles leaving the thruster through the extraction grid to the amount of particle inflow through the inlet nozzle. The particles leaving the thruster are either singly charged ions or atoms. The thrust producing ion flux is commonly expressed as a beam current,

$$I_\mathrm{b} = e h_\mathrm{grid} n_\mathrm{e} u_\mathrm{B} A_\mathrm{grid} \alpha_\mathrm{i}, \tag{11}$$

with $h_\mathrm{grid} n_\mathrm{e}$ representing the charge carrier density at the grid boundary of the simulation domain, A_grid representing the grid area, and α_i representing the transparency of the extraction grid system for ions [28]. Since α_i is not known a priori and since no particle tracking code is used, an additional loop not shown in Fig. 2 starts with a guess, and the parameter is iteratively updated until the deposited power matches the experimentally obtained power measured within the resonant circuit. This methodology is validated by the ChildâĂŞLangmuir law, which predicts the maximum achievable current in the case of spacecharge limited conditions. The additional loop iteratively processes the complete model shown in Fig. 2. Convergence is achieved by a proportional-integral controlling scheme that adjusts the ion transparency iteratively according to

$$\alpha_\mathrm{i}^j = \alpha_\mathrm{i}^{j-1} - \alpha_\mathrm{i}^{j-1}\left[k_\mathrm{P}\left(P_\mathrm{exp} - P^{j-1}\right) + k_\mathrm{I}\sum_{n=1}^{j-1}\left(P_\mathrm{exp} - P^n\right)\right], \tag{12}$$

with superscript j denoting the iterative step number, k_P and k_I denoting the proportional and integral control constants, respectively, P_j denoting the numerically obtained power at iteration j, and P_exp denoting the experimentally obtained power. To prevent the iterative solution from over- and undershooting, which may cause severe stability issues due to the nonlinear behavior of the plasma, k_P and k_I are chosen to be on the order of 10^{-3}.

To close the loop, the amount of neutral gas leaving the thruster γ_n is also calculated as shown in [13,14]. This allows for determination of the mass usage efficiency

$$\eta_\mathrm{m} = \frac{I_\mathrm{b}}{I_\mathrm{b} + e\gamma_\mathrm{n}}. \tag{13}$$

The definition of the mass usage efficiency used in this work is based on singly ionized species only and accounts for the ionized vs un-ionized propellant [14].

E. Thruster Impedance and Propulsive Performance

After convergence of the conservation equations, the self-consistent loop is finished, and physically meaningful results are obtained. From those converged parameters, the thruster impedance can be derived. The Poynting theorem for time-harmonic fields, neglecting the radiative term due to a large wavelength compared to the coilâĂŹs size, is used to evaluate the lumped circuit elements' values that are used to describe the discharge on a global scale as defined in Fig. 1 [26]:

$$\frac{1}{2}\widetilde{I}^{*}\widetilde{V} = \frac{1}{2}\iiint_V \left|\widetilde{\mathbf{E}}\right|^2 \kappa_\mathrm{p}\,\mathrm{d}V + 2\mathrm{i}\omega \iiint_V \left(u_\mathrm{e} - u_\mathrm{m}\right)\,\mathrm{d}V \tag{14}$$

In this equation, the asterisk denotes the complex conjugate of a quantity, and u_e and u_m denote electric and magnetic energy density, respectively. Those energy densities can be derived from the electromagnetic fields defined earlier. The resistive and reactive components of the load impedance can be derived from Eq. (14).

Furthermore, the propulsive performance of the thruster such as thrust and specific impulse can be obtained from the converged solution. Taking the mean kinetic velocity of neutrals v_n and the electrostatically accelerated velocity of ions $v_\mathrm{i} = (2eV_\mathrm{scr}/m_\mathrm{i})^{1/2}$ and their respective fluxes leaving the thruster into account, and assuming $m_\mathrm{i} \approx m_\mathrm{n}$, the total thrust is obtained:

$$T = m_\mathrm{i}\left(\gamma_\mathrm{i} v_\mathrm{i} + \gamma_\mathrm{n} v_\mathrm{n}\right) \tag{15}$$

The specific impulse can finally be calculated to

$$I_\mathrm{sp} = \frac{v_\mathrm{eff}}{g_0}, \tag{16}$$

with the effective exhaust velocity $v_\mathrm{eff} = T/m_\mathrm{i}\left(\gamma_\mathrm{i} + \gamma_\mathrm{n}\right)$ and standard gravity g_0 [16].

III. Experiment

The experimental setup for *in-situ* power measurement is schematically shown in Fig. 3. An Octiv VI probe from Impedans, Ltd., is used. Because of its patented spectrum-averaging methodology [29], it offers high phase stability and nominal resolution down to 0.01 deg. It, furthermore, offers phase-resolved voltage and current measurement up to several hundred megahertz and exhibits hardly any insertion loss (manufacturer's definition: 0.1 dB) into the circuit under test. Voltage and current signals are collected by capacitive and inductive pickup circuits, respectively, without distorting the RF waveform. The collected signals are digitized in an analog-to-digital converter (ADC) and then processed within the Octiv logic, which is implemented in a field programmable gate array, facilitating high-speed applications. The logic uses a fast Fourier transform (FFT) to convert the collected signals to the frequency domain, in which the previously mentioned spectrum averaging is performed. For that purpose, the time signal is organized into blocks of equal lengths (on the order of microseconds). Each block of data is then processed by the FFT algorithm with a special signal windowing function to reduce spectral spreading. The obtained rms voltage, rms current, phase, forwarded power, and reflected power values are then forwarded to a software that offers several methods of visualization of the data.

Impedans calibrates each device to traceable standards. A detailed description of its standards of calibration can be found in [30]. The calibration ensures voltage, current, and power measurement accuracy of $\pm 1\,\%$; frequency accuracy of $\pm 10\,\mathrm{kHz}$; and phase accuracy of $\pm 1\,\mathrm{deg}$.

For validation, a test without the probe was performed before the power measurement. No change in thruster performance, i.e., DC power consumption or any other parameters such as thrust and ion beam current, was observed. Additionally, there was no change of the resonant frequency by the RFG after inserting the probe, which confirms that the probe does not significantly change the load. Unfortunately, the RFG is not capable of measuring RF power at its output terminal. Before the experiment, complex dummy loads were powered with the RFG, and the signals were measured with the Octiv. The resulting impedances were in excellent agreement with LCR meter measurements.

The coaxial feed cables slightly change the source and load impedance. However, because of the short cable lengths, this effect is assumed negligible for the assessment of power distribution.

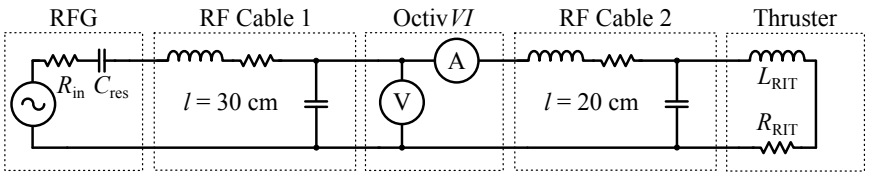

Fig. 3 Schematic diagram of the experimental setup. Input and load impedance are slightly altered due to parasitic RF cable impedance.

Table 1 Thruster modes for numerical and experimental investigation.

	V_{scr}	V_{acc}	I_b
Mode 1:	1800 V	−300 V	9.97 mA
Mode 2:	1800 V	−300 V	15.25 mA

The reactance of the RG 213 cables used in this setup is primarily of the inductive type since the load is typically driven at around 2 MHz. Hence, $1/\omega C \gg \omega L$, with C denoting the cables' capacitance, which is on the order of several $\mathrm{pF\,m^{-1}}$, and L denoting their inductance on the order of $100\,\mathrm{nH\,m^{-1}}$ (nanohenries per meter). Based on that, there is substantially no current driven through the capacitive shunt. Additionally, ohmic losses are on the order of several $\mathrm{m\Omega\,m^{-1}}$ (milliohms per meter), and thus no significant power consumption of the cables is expected.

Once the RFG has matched the load by tuning its frequency to the resonant frequency

$$\omega_0 = \frac{1}{\sqrt{(L + L_{RIT})\, C_{res}}} \tag{17}$$

the reactances cancel each other, leaving only the ohmic components R_{in} and R_{RIT}. The relation of those resistances determines the power forwarded to the thruster and thus the plasma discharge. The signals within the resonant circuit are continuously captured using the Octiv VI probe. Because of the characteristics of the resonant circuit, the current and the voltage signals' values are amplified with respect to the DC input's values. From those signals, all the important quantities like impedance, coupled power, and coupling efficiency are derived.

The experiments were performed in the high-vacuum plume test facility for electric thrusters (ET) (STG) at the Spacecraft Department of the German Aerospace Center in Goettingen, Germany. The facility offers realistic environmental conditions for electric thrusters due to its size and the achievable base pressure. The chamber is cylindrical, with 12.2 m in axial length and 5 m in diameter, resulting in a total volume of approximately 230,000 L, taking the curvature of the lids into account. A schematic of the chamber is shown in Fig. 4. A detailed description of the facility including thrust, plasma, and ion beam diagnostics is given in [31,32].

The pumping arrangement, consisting of four rough vacuum pumps, four turbo molecular pumps, and ten cryogenic pumps, each 50 cm in diameter, was designed to achieve a base pressure in the low 10^{-7} mbar range. The pumping speed on cold xenon gas was approximately $130,000\,\mathrm{L\,s^{-1}}$ (liters per second). The pressure gauges were installed symmetrically around the thruster exit as suggested in [33].

The pumping arrangement, consisting of four rough vacuum pumps, four turbo molecular pumps and ten cryogenic pumps, each 50 cm in diameter, is designed to achieve a base pressure in the low 10^{-7} mbar range. The pumping speed on cold xenon gas is approximately $130,000\,\mathrm{L\,s^{-1}}$. The pressure gauges are installed symmetrically around the thruster exit as suggested in [33].

IV. Results

Two different sets of input parameters are investigated here. The parameter sets, corresponding to two modes, are defined by the screen grid voltage V_{scr}, the acceleration grid voltage V_{acc}, and the ion beam current I_b. For each mode, the acceleration grid current I_{acc} was well below 1 % of the screen grid current I_{scr}, leading to $I_b = I_{scr} - I_{acc} \approx I_{scr}$. The modes of thruster operation are shown in Table 1.

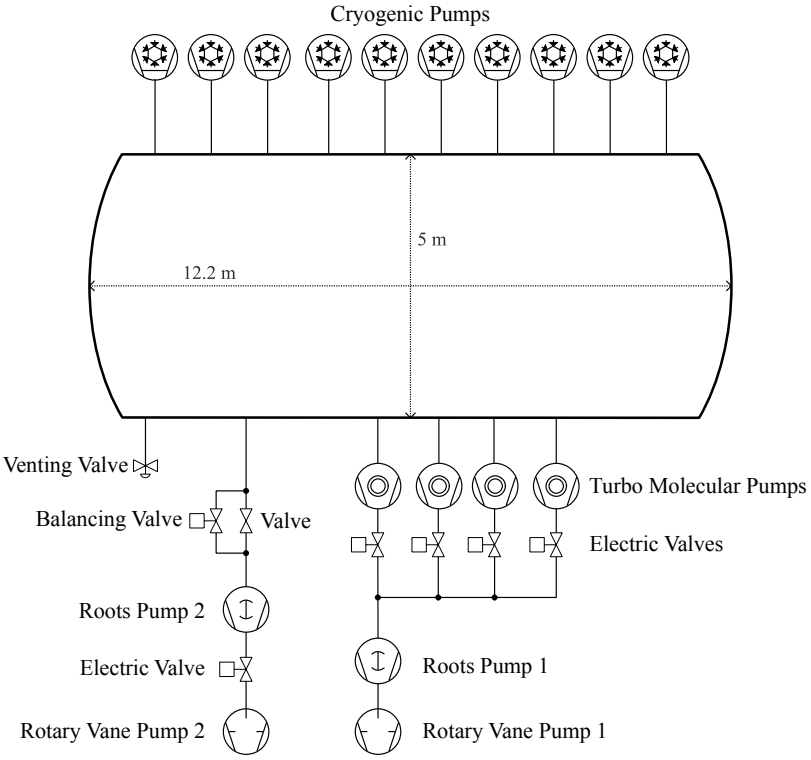

Fig. 4 Schematic drawing of the vacuum facility STG ET with pumping layout.

Both the simulation and experiment were performed with those modes. In mode 1, the neutral xenon volumetric inflow rate was varied from $\dot{V} = 1 \ldots 10\,\mathrm{sccm}$. Because of instabilities at higher mass flow, the inflow rate in mode 2 was limited to $\dot{V} = 1 \ldots 8\,\mathrm{sccm}$.

The thruster used for this work was a RIT-10/37 engine developed by the University of Giessen and distributed by TransMIT, GmbH. It is composed of a discharge chamber with 10 cm in diameter and an extraction system with 37 beamlets. The nominal thrust level of this thruster lies in the lower single-digit millinewton range.

In the following, some numerically obtained results are shown to give an overviewof the plasma parameters as well as the performance of the thruster. First, the electromagnetic fields and the plasma current and charge carrier density inside the simulation domain are presented in Figs. 5a-5d. A typical simulation result, corresponding to the case of $\dot{V} = 1\,\mathrm{sccm}$ in mode 1 is shown.

An influence of the conductive structures of the thruster on the field distributions can be observed. Especially, the gas inlet, which is composed of solid titanium, seems to have a measurable effect on the electric field, as depicted in Fig. 5a in terms of the distortion of the field lines. The electric field does not penetrate into the highly conductive metal. Instead, it is distorted, and eddy currents are induced at the material's surface. Those influences will ultimately lead to increased eddy losses and thus alter the power distribution within the thruster.

It is also interesting to study the magnetic field inside the plasma (Fig. 5b). The magnetic field lines encircle the peak value of the plasma current density. The peak is localized near the radial wall of the discharge chamber due to the location of the induction coil (Fig. 5c).

The charge carrier density distribution, as depicted in Fig. 5d, follows the parabolic profile defined in Eq. (10). A discontinuity at the edge of the gas inlet is observable. This is due to erroneous implementation of the profile. Specifically, the excess length of the gas inlet into the discharge chamber was not taken into account when the shape of the density profile was modeled. However, since this region is not effectively heated by the electromagnetic fields, as can be concluded from Fig. 5c, no substantial impact on the converged solution of the plasma parameters is anticipated. This assumption was proven valid by manually tuning the density values in the corresponding area

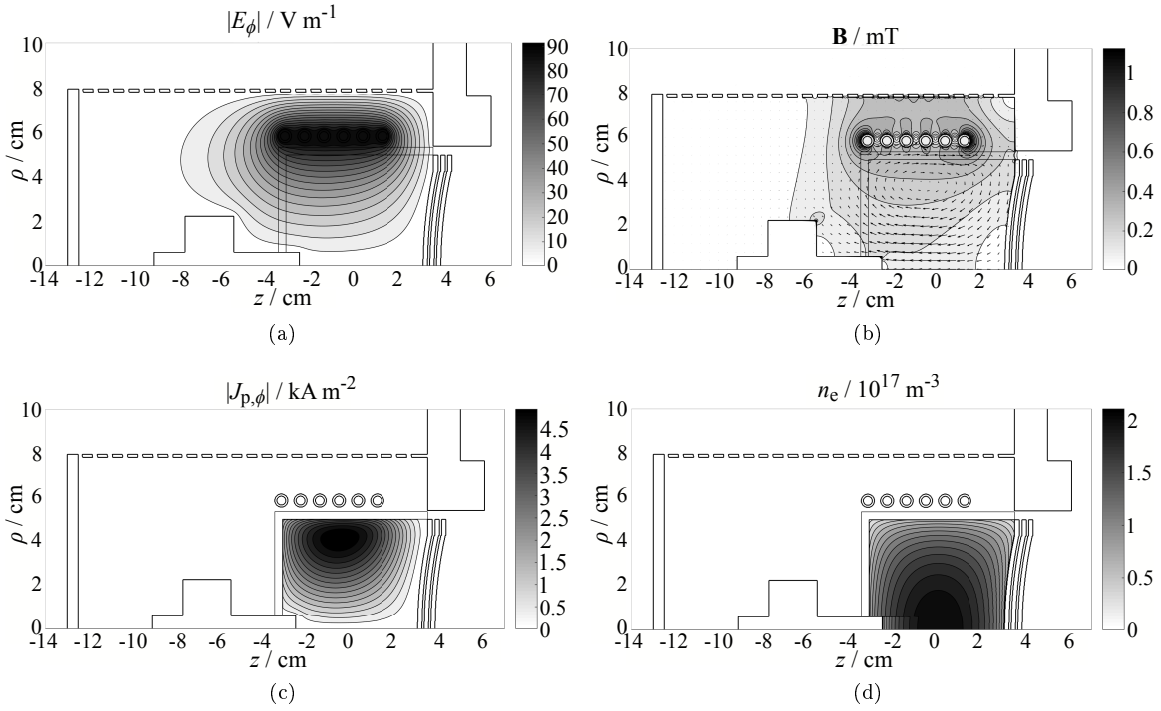

Fig. 5 a) Electric and b) magnetic field distribution, c) plasma current density, and d) charge carrier density for $\dot{V} = 1\,\mathrm{sccm}$ in mode 1.

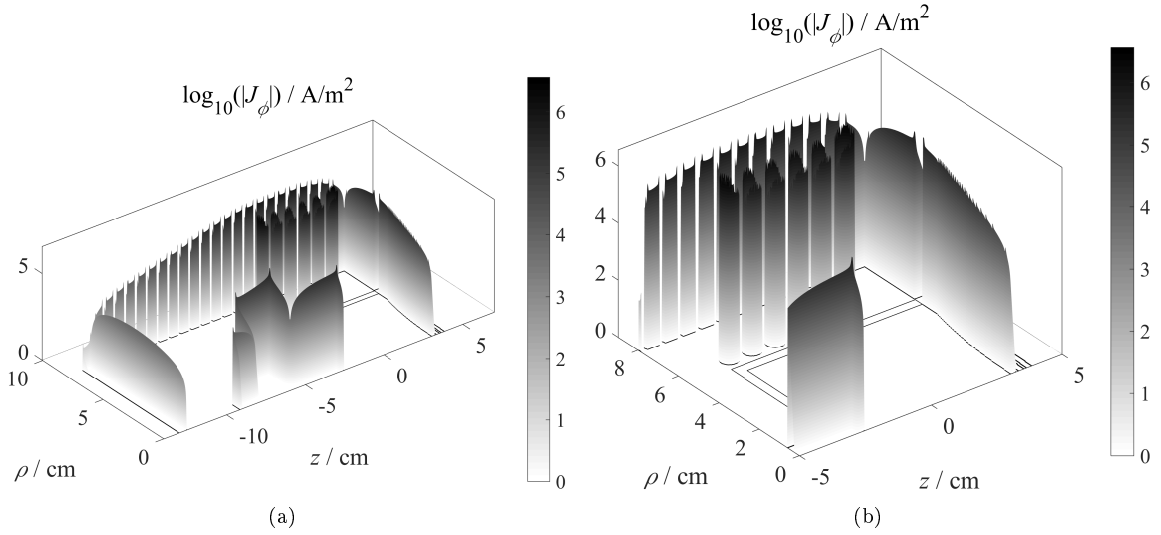

Fig. 6 Current density on a log scale, a) inside the structural components of the thruster and b) zoomed-in view.

without any measurable effects. However, for the sake of integrity, the implementation will be fixed with the next update of the simulation code.

Another important physical effect that can be investigated with aid of the model is the proximity effect in the coil wire, which is depicted in terms of the current density inside the conductive structures in Fig. 6. This effect is caused by the current density inside adjacent coil windings. The magnetic fields caused by those currents compensate each other between the windings and hence displace the current density to regions of low nominal opposing field strengths. This effect, in contrast to the well-understood skin effect, is nearly impossible to account for analytically, since

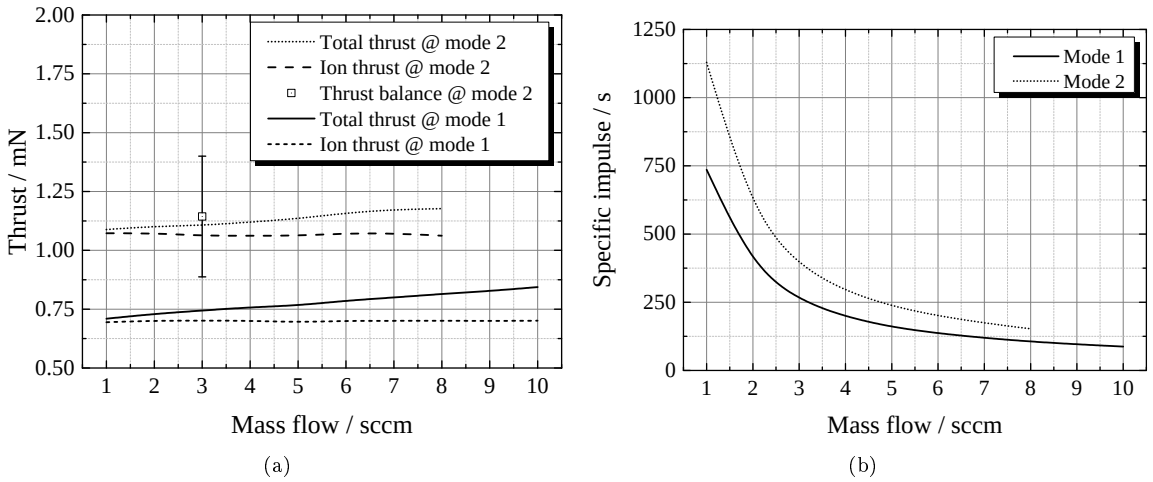

Fig. 7 (a) Thrust and b) specific impulse of the RIT-10/37 thruster in operation modes 1 and 2. The thrust was measured at$\dot{V} = 3$ sccm in mode 2.

it is a strong function of geometry. A very realistic current distribution, which again influences the coupling of energy from coil to plasma, can be derived with this functionality. It is thus considered extremely valuable to account for the proximity effect in RIT simulations.

Thrust and specific impulse of modes 1 and 2 are shown in Figs. 7a and 7b, respectively.An inverted pendulum thrust balance manufactured by Advanced Space Technologies GmbH was used to measure the thrust at one nominal operating point ($\dot{V} = 3$ sccm in mode 2). It shows large error bars in the lower millinewton range since it was designed for higher thrust levels up to 250 mN [31]. It is only used here to perform a plausibility check of the model.

Figure 7a shows the ion thrust for modes 1 and 2, which is held constant by the parameters defined in Table 1. Furthermore, the impact of the neutral gas leaving the thruster can be determined with aid of the self-consistent model. The curves show that, especially in areas of low thrust, as is the case with the RIT-10/37, there is a significant contribution of neutrals to the overall delivered thrust. The influence of the neutral gas flow is also depicted in Fig. 7b in terms of I_{sp}. The thruster under the test has relatively few extraction apertures and hence is not optimized for high I_{sp} applications as is typically the case for RITs. However, even using this nonideal grid system, an $I_{\mathrm{sp}} \approx 2000$ s may be achieved by setting the flow rate $\dot{V} < 1$ sccm. Unfortunately, the mass flow controller used for this study showed unstable behavior in this range and could not be used to generate further data points at the lower flow rates.

The thruster assembly DC power consumption (including generator and RF cables) as well as the forwarded power at the thruster coil are shown in Fig. 8. It can be seen that at flow rates below 2 sccm the forwarded power decreases while the DC input still increases. That is attributed to the impedance bridge mismatch introduced in Sec. I.A and is regarded as a new design parameter for the assembly of an electric propulsion system based on RIT. Overall, the DC power consumption of a RIT assembly not only correlates to discharge but also circuit parameters following $P_{\mathrm{DC}} = f\left(I_{\mathrm{scr}}, \dot{V}, \eta\right)$. Those parameters again depend on other discharge parameters as shown in Sec. II.

The error bars in Fig. 8 are due to measurement inaccuracy of the grid current data acquisition, which is based on a 10 bit ADC. The resolution of the PHV voltage supply attached to the screen grid is 0.59 mA, which manifests in fairly high uncertainty when going down to low beam currents. With $P_{\mathrm{DC}}, P_{\mathrm{RF}} \propto I_{\mathrm{scr}}$, it follows that $\Delta P_{\mathrm{RF}} \propto \Delta I_{\mathrm{scr}}$, with Δ being the absolute error. Essentially, the same behavior is seen at the measured resonant coil current $I_{\mathrm{RF}} = \left|\widetilde{I}_{\mathrm{RF}}\right| = \left(P_{\mathrm{RF}}/R_{\mathrm{RIT}}\right)^{1/2}$, as depicted in Fig. 9.

There is an observable deviation between the coil currents calculated by the model and the measured values that is mainly due to the plasma discharge being modeled using continuum methods. This conclusion is supported by the development of the deviation (dashed lines in Figs. 9a and 9b), which decreases at higher flow rates. The coil current is the most important figure of merit in terms

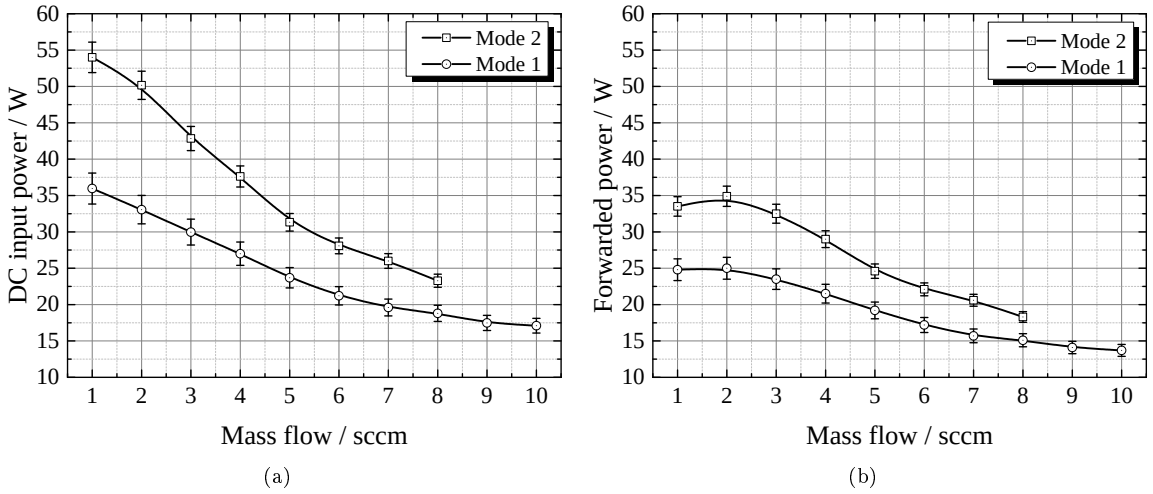

Fig. 8 (a) Measured DC power consumption and (b) measured forwarded RF power.

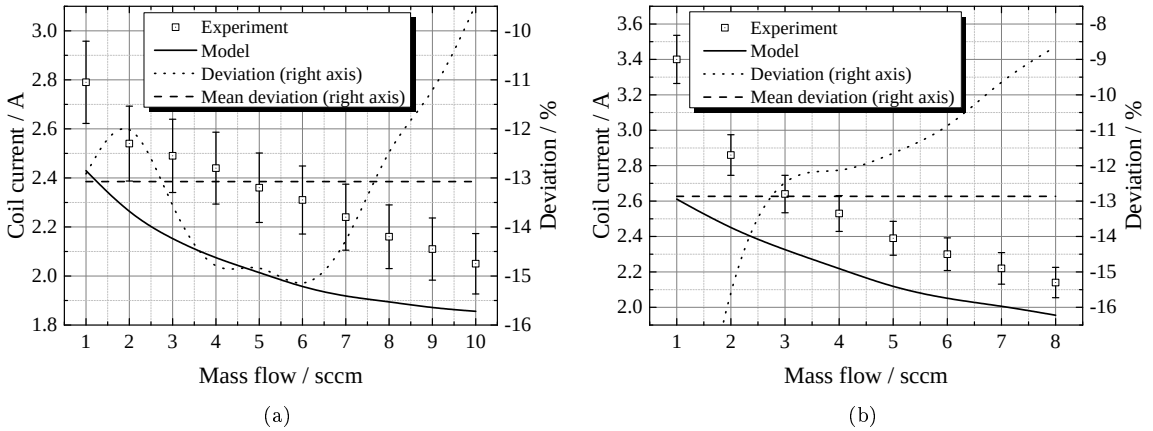

Fig. 9 Experimentally and numerically obtained coil currents for a) mode 1 and b) mode 2. The mean deviation of the model is approximately 13 % below the measured values.

of the accuracy of the model. Since the model is adjusted with measured power values, this power (along with the other input parameters) is used to determine the coil current as well as the thruster resistance R_{RIT} iteratively. At the circuit level, under the assumption of purely ohmic impedance, which holds true because the thruster is driven in resonant mode, Eq. (14) essentially simplifies to $P = I^2 R_{\mathrm{RIT}}$, with I denoting the coil current. It is therefore very important to have at least an acceptable agreement of numerically and experimentally obtained current values to justify the correct output of the plasma model (charge carrier density and electron temperature), which again are used to correctly determine power distribution and any derived quantities.

Since the coil current is an integral quantity, it does not directly correlate to local power dissipation within the thruster. But it can be related to changes in the plasma, and those can be stimulated by the input parameters, which affect those local distributions that in turn can be attributed to the particular terms in Eq. (14). This equation essentially is a conservation equation for electrical energy.

The Knudsen number $\mathrm{Kn} = \lambda/l$, with the mean free path between collisions λ and the circumference of the discharge chamber l, is also shown in Fig. 10a. The range of data clearly shows that the rarefication of gas particles within the discharge lies between absolutely rarefied ($\mathrm{Kn} \geq 10$) and continuum ($\mathrm{Kn} < 0.1$). This area is also referred to as the transition regime. Given the simplicity of the proposed model and thus the short simulation duration of only a few minutes per data point, the

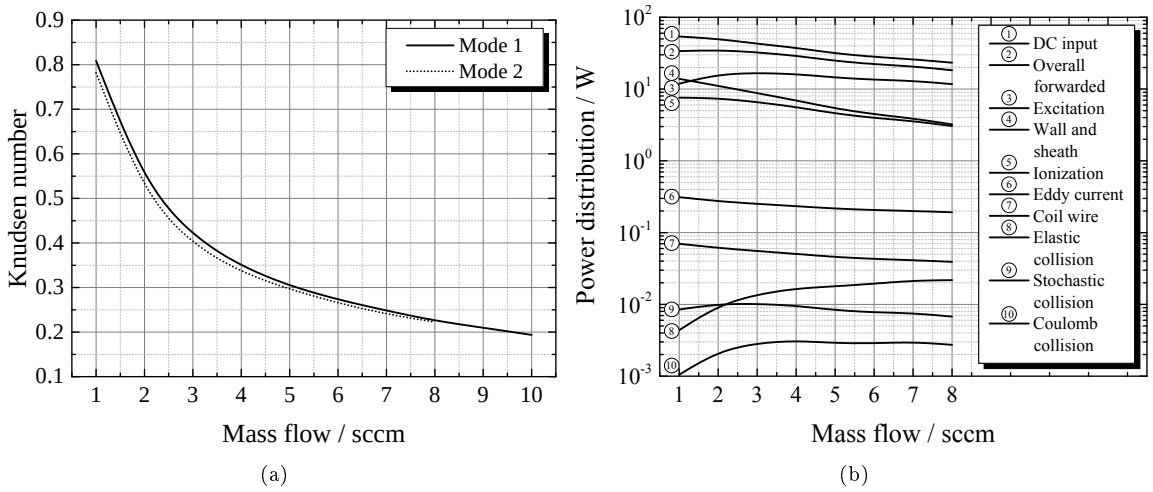

Fig. 10 a) Knudsen numbers for modes 1 and 2 and b) the power distribution for mode 2.

deviation is acceptable. More accurate results could be obtained by using a free molecular kinetic type of code like DSMC [34]. This would imply long simulation times and is thus not the scope of this work because simulation duration is considered a crucial aspect for engineering purposes.

The power distribution within the thruster, including structural losses, is depicted in Fig. 10b. It is observable that a significant amount of power is lost to excitation processes, especially when going to higher mass flows. This behavior is expected due to increasing pressure inside the discharge chamber and hence decreasing mean free length between collisions. At very low pressure, as indicated in the figure below 2 sccm, the electron energy is high enough to ionize a particle instead of exciting it to a higher energy state. This can happen because electrons can gain sufficient energy from the accelerating electric field due to the very large mean free path between collisions. This is also observed in the experiment. The discharge appears darker at lower flow rates. Since the extracted number of ions is kept constant, as a result, there is less excitation and hence fewer radiative transitions. For further information, the cross-sections of the corresponding processes should be assessed [23].

It is furthermore expected that eddy current losses inside the thruster might be higher in reality. Since the geometric representation is merely an approximation of the actual thruster, some features like screws, sharp edges, and other irregularities are not considered at the moment. In the next release, the model will be updated to be capable of importing CAD drawings, which is anticipated to describe structural losses more realistically.

The numerically obtained thrust from Fig. 7a together with the measured forwarded and DC power are used to introduce the PTTR in Fig. 11a. It can be seen that the PTTR in case of DC power increases with lower mass flows. In contrast to that, the PTTR based on the actual forwarded power decreases with decreases in mass flow. This is due to the aforementioned mismatch of the impedance bridge between the RFG and thruster. Figure 11b shows this mismatch in terms of coupling efficiency. As can be observed in the inset, the resistance of the load strongly decreases when approaching low mass flow rates. This decrease leads to an electrically adverse relation between source and load resistance, which again results in power loss within the generator.

V. Conclusion

This paper presented a concise approach based on experimental and numerical studies to distinguish between power absorption at the assembly and the thruster level. The power consumption of the assembly, prominently consisting of the thruster, the RFG, and feeding cables, has to be interpreted with great care due to effects like impedance bridge mismatch. Power lost to this channel is often attributed to effects inside the thruster, or the plasma, and thus may lead to miscalculation of actual thruster performance. An applicable example is given by the PTTR. This paper showed that, especially in areas of low mass flow, which are common in space missions due to longevity, there is

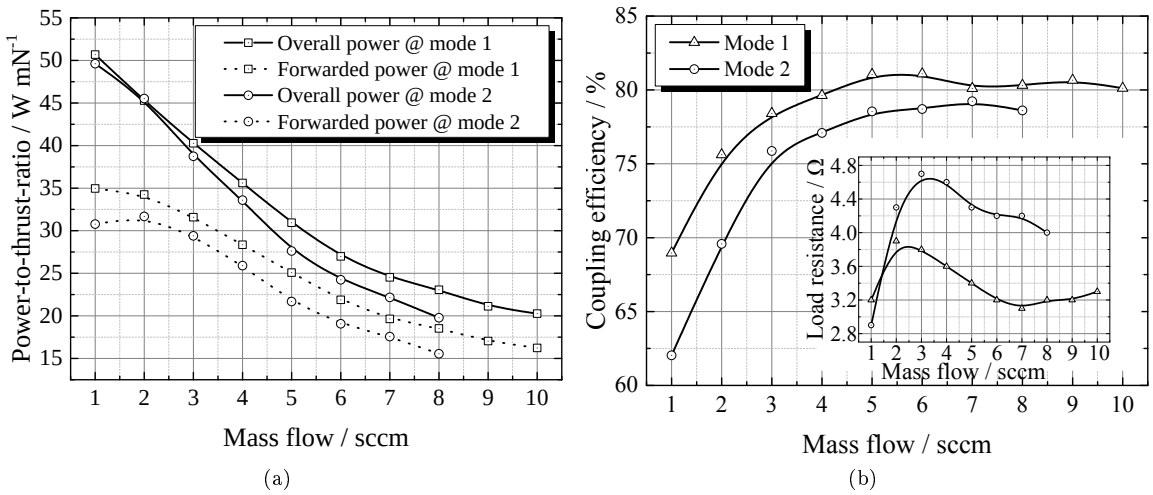

Fig. 11 a) PTTR and b) load coupling efficiency. The inset in b shows the measured load resistance.

a difference of about $30 - 40\,\%$ between DC input and forwarded RF power. This information can furthermore be used for thermal modeling of the assembly.

The model used in this work was based on a continuum approach to modeling the plasma discharge. It is considered adequate because the sources of error are well understood and the error itself lies in acceptable areas. The identified errors were reported and discussed, and appropriate solution approaches were suggested. A major advantage of the model is its simulation time, which is on the scale of minutes per working point. Because of that, the model can be used as a virtual prototype, which is considered beneficial for optimization strategies during thruster development.

The experimental setup was based on a phase-resolved voltage and current meter as well as the thruster assembly including all the necessary peripherals. Because of the low resolution of the extracted ion current measurement, there is a nonnegligible error associated with this parameter. This is an unfortunate fact that will be assessed by high-resolution ADCs and/or an optimized extraction grid that allows for more ion current to be extracted. The latter requires a RFG that is capable of power levels up to several hundred watts that is currently under development.

The hybrid approach presented, consisting of power measurement and postprocessed simulation, offers detailed insight into the plasma physics within the inductive discharge. With this methodology, the integral telemetry data during measurement can be matched to actual processes inside the discharge. It is believed that this methodology is crucial for efficient optimization of RIT assemblies. Furthermore, this paper clearly showed the necessity of power measurement near the inductive load instead of using input DC power values, as mentioned earlier in terms of the PTTR.

References

[1] Killinger, R., Kukies, R., Surauer, M., Tomasetto A., and van Holtz, L., "ARTEMIS Orbit Raising Inflight Experience with Ion Propulsion", *Acta Astronautica*, Vol. 53, 2003, pp. 607-621.
doi: 10.1016/SOO94-5765(03)00168-l

[2] Martinez-Sanchez, M. and Pollard, J. E., "Spacecraft Electric Propulsion–An Overview", *Journal of Propulsion and Power*, Vol. 14, No. 5, 1998, pp. 688-699.
doi: 10.2514/2.5331

[3] Rayman, M. D. and Williams, S. N., "Design of the First Interplanetary Solar Electric Propulsion Mission", *Journal of Spacecraft and Rockets*, Vol. 39, No. 4, 2002, pp. 589-595.
doi: 10.2514/2.3848

[4] Mazouffre, S., "Electric Propulsion for Satellites and Spacecraft: Established Technologies and Novel Approaches", *Plasma Sources Science and Technology*, Vol. 25, No. 3, 2016, Article 033002.

doi: 10.1088/0963-0252/25/3/033002

[5] Hutchins, M., Simpson, H. and Jimenez, J. P., "QinetiQ's T6 and T5 Ion Thruster Electric Propulsion System Architectures and Performances", *Proceedings of the 34th International Electric Propulsion Conference*, Hyogo-Kobe, Japan, 2015, Proceeding IEPC-2015-131.

[6] Simon, J., Probst, U. and Klar, P. J., "Development of a Radio-Frequency Generator for RF Ion Thrusters", *Transactions of the Japan Society for Aeronautical and Space Sciences, Aerospace Technology*, Vol. 14, No. ists30, 2016, Article Pb_33.
doi: 10.2322/tastj.14.Pb_33

[7] Leiter, H. J, Loeb, H. W. and Schartner, K.-H., "The RIT-15 Ion Engines–A Survey of the Present State of Radio Frequency Ion Thruster Technology and its Future Potentiality", *Third International Conference on Spacecraft Propulsion*, Cannes, France, 2000, pp. 423-432.

[8] Bassner, H., Killinger, R., Leiter, H. and Mueller, J., "Development Steps of the RF-Ion Thrusters RIT", *Proceedings of the 27th International Electric Propulsion Conference*, Passadena, USA, 2001, Proceeding IEPC-2001-105.

[9] Erickson, R. W. and Maksimovic, D., *Fundamentals of Power Electronics*, 2nd ed., Springer US, New York, USA, 2001.

[10] Bowick, C., Blyler, J. and Ajluni, C., *RF Circuit Design*, 2nd ed., Newnes, Pennsylvania, USA, 2007.

[11] de Silva, C. W., *Sensor Systems: Fundamentals and Applications*, CRC Press, Florida, USA, 2016.

[12] Simon, J., Volkmar, C. and Probst, U., "High-Precision Power Measurement for Accurate Characterization of RF Ion Thrusters", *Proceedings of the 5th International Conference on Space Propulsion*, Rome, Italy, 2016, Proceeding SP2016_3124614.

[13] Volkmar, C. and Ricklefs, U., "Implementation and Verification of a Hybrid Performance and Impedance Model of Gridded Radio-Frequency Ion Thrusters", *European Physical Journal D*, Vol. 69, 2015, Article 227.
doi: 10.1140/epjd/e2015-60380-4

[14] Volkmar, C., Ricklefs, U. and Klar, P. J., "Self-Consistent Numerical 0D/3D Hybrid Modeling of Radio-Frequency Ion Thrusters", *Transactions of the Japan Society for Aeronautical and Space Sciences, Aerospace Technology*, Vol. 14, No. ists30, 2016, Article Pb_23.
doi: 10.2322/tastj.14.Pb_23

[15] Lieberman, M. A. and Lichtenberg, A. J., *Principles of Plasma Discharges and Materials Processing*, 2nd ed., Wiley, New Jersey, USA, 2005.

[16] Goebel, D. M. and Katz, I., *Fundamentals of Electric Propulsion: Ion and Hall Thrusters*, 1st ed., Wiley, New Jersey, USA, 2008.

[17] Chabert, P. and Braithwaite, N. S. J., *Physics of Radio-Frequency Plasmas*, 1st ed., Cambridge University Press, New York, USA, 2011.

[18] Goebel, D. M., "Analytical Discharge Model for RF Ion Thrusters", *IEEE Transactions on Plasma Science*, Vol. 36, 2008, pp. 2111-2121.
doi: 10.1109/TPS.2008.2004232

[19] Chabert, P., Monreal, J. A., Bredin, J., Popelier, L. and Aanesland, A., "Global Model of a Gridded-Ion Thruster Powered by a Radiofrequency Inductive Coil", *Physics of Plasmas*, Vol. 19, 2012, Article 073512.
doi: 10.1063/1.4737114

[20] Tsay, M. M. and Martinez-Sanchez, M., "Simple Performance Modeling of a Radio-Frequency Ion Thruster", *Proceedings of the 30th International Electric Propulsion Conference*, Florence, Italy, 2007, Proceeding IEPC-2007-072.

[21] Turkoz, E. and Celik, M., "2-D Electromagnetic and Fluid Models for Inductively Coupled Plasma for RF Ion Thruster Performance Evaluation", *IEEE Transactions on Plasma Science*, Vol. 42, 2014,

pp. 235-240.
doi: 10.1109/TPS.2013.2287903

[22] Lee, C. and Lieberman, M. A., "Global Model of Ar, O2, Cl2, and Ar/O2 Highdensity Plasma Discharges", *Journal of Vacuum Science and Technology A*, Vol. 13, 1995, pp. 368-380.
doi: 10.1116/1.579366

[23] Hayashi, M., "Bibliography of Electron and Photon Cross Sections with Atoms and Molecules Published in the 20th Century– Xenon–", NIFS, NIFS-DATA-79, 2003.

[24] Hayashi, M., "Determination of Electron-Xenon Total Excitation Cross-Sections, from Threshold to 100 eV, from Experimental Values of Townsend's α", *Journal of Physics D: Applied Physics*, Vol. 16, 1983, pp. 581-589.
doi: 10.1088/0022-3727/16/4/018

[25] Godyak, V. A., Piejak, R. B. and Alexandrovich, B. M., "Electron Energy Distribution Function Measurements and Plasma Parameters in Inductively Coupled Argon Plasma", *Plasma Sources Science and Technology*, Vol. 11, 2002, pp. 525-543.
doi: 10.1088/0963-0252/11/4/320

[26] Jackson, J. D., *Classical Electrodynamics*, 3rd ed., Wiley, New Jersey, USA, 1998.

[27] Dobkevicius, M. and Feili, D., "A Coupled Performance and Thermal Model for Radio-Frequency Gridded Ion Thrusters", *European Physical Journal D*, Vol. 70, 2016, Article 227.
doi: 10.1140/epjd/e2016-70273-7

[28] Farnell, C. C., "Performance and Lifetime Simulation of Ion Thruster Optics", PhD Dissertation, Colorado State University, USA, 2007.

[29] Scullin, P. and Hopkins, M., "Analysing RF Signals from a Plasma System", Patent WO 2014016357 A3, 2014.

[30] Lennon, J., Poghosyan, T., Gahan, D., Scullin, P. and Hopkins, M. B., "Octiv VI Technology - Standards of Calibration", Technical Note [OC04], `https://impedans.com/sites/default/files/pdf_downloads/oc04_octiv_vi_technology_-_standards_of_calibration.pdf`.

[31] Neumann, A., "STG-ET: DLR Electric Propulsion Test Facility", *Journal of Large-Scale Research Facilities JLSRF*, Vol. 3, 2017, Article A108.
doi: 10.17815/jlsrf-3-156

[32] Neumann, A., "Update on Diagnostics for DLR's Electric Propulsion Test Facility", *Procedia Engineering*, Vol. 185, 2017, pp. 47-52.
doi: 10.1016/j.proeng.2017.03.289

[33] Dankanich, J. W., Walker, M., Swiatek, M. W. and Yim, J. T., "Recommended Practice for Pressure Measurement and Calculation of Effective Pumping Speed in Electric Propulsion Testing", *Journal of Propulsion and Power*, Vol. 33, No. 3, 2017, pp. 668-680.
doi: 10.2514/1.B35478

[34] Bird, G. A., *Molecular Gas Dynamics and the Direct Simulation of Gas Flows*, 2nd ed., Clarendon Press, Oxford, UK, 1994.